JGR Solid Earth

RESEARCH ARTICLE
10.1029/2019JB018540

Key Points:
- Fundamental-mode Rayleigh waves are affected by major-arc overtone interference, resulting in oscillations in phase and amplitude
- Interference is strongest at path lengths between 120-160 degrees; stations in/around the Atlantic basin likely exhibit the largest bias.
- The interference explains greater measurement misfit at large path lengths but has a minor effect on aggregate phase-velocity maps.

Supporting Information:
- Supporting Information S1

Correspondence to:
A. Hariharan,
anant_hariharan@brown.edu

Citation:
Hariharan, A., Dalton, C. A., Ma, Z., & Ekström, G. (2020). Evidence of overtone interference in fundamental-mode rayleigh wave phase and amplitude measurements. *Journal of Geophysical Research: Solid Earth*, *125*, e2019JB018540. https://doi.org/10.1029/2019JB018540

Received 14 AUG 2019
Accepted 7 DEC 2019
Accepted article online 10 DEC 2019

Evidence of Overtone Interference in Fundamental-Mode Rayleigh Wave Phase and Amplitude Measurements

Anant Hariharan[1], Colleen A. Dalton[1], Zhitu Ma[2], and Göran Ekström[3]

[1]Brown University, Department of Earth, Environmental, and Planetary Sciences, United States, [2]Tongji University, School of Ocean and Earth Science, China, [3]Lamont-Doherty Earth Observatory of Columbia University, United States

Abstract We present evidence that measurements of minor-arc fundamental-mode (FM) Rayleigh waves experience interference from major-arc overtones, resulting in travel-time and amplitude measurements oscillating along a ray path. The oscillations are present in synthetic seismograms generated in a 3-D Earth model via SPECFEM3D_GLOBE and in a 1-D Earth model by mode summation. The absence of oscillations in synthetics containing only the FM indicates that the oscillations originate from higher-mode interference. This interference is present across multiple measurement techniques, including multi-channel cross correlation, phase-matched filtering, and cluster analysis. Experiments with 1-D synthetics suggest that contamination from interference is largest at epicentral distances greater than around 120 degrees, where record sections of seismograms show the major-arc overtones intersecting the minor-arc FM Rayleigh wave. The short wavelength of the interference pattern means it is only observable with dense station spacing and high data quality, which may explain why it has not, to our knowledge, been previously recognized. We show the interference is visible in real data. Its overall impact on phase-velocity maps is probably minor due to many measurements from shorter path lengths less prone to interference bias. However, phase-velocity maps constructed only from measurements at epicentral distances prone to interference exhibit significant noise and poor agreement with maps from measurements that include all path lengths; the issue is especially problematic for approaches that use differential travel times between nearby stations. Accounting for interference may diminish noise in measurements and improve the accuracy of images of the upper mantle.

1. Introduction

Fundamental-mode (FM) Rayleigh wave measurements provide unique and critical information for imaging the seismic structure of the upper mantle. Rayleigh waves are clear on the vertical component of seismograms, well separated from other seismic arrivals, and well dispersed in frequency. Their depth sensitivity to shear velocity depends strongly on period, providing constraints on seismic structure at depths < 300 km. As a result of these properties and the good lateral coverage of surface-wave paths, FM Rayleigh wave measurements form the basis of many global (Ritsema et al., 2011; Shapiro & Ritzwoller, 2002; Zhou et al., 2006) and regional (Shen & Ritzwoller, 2016; Wagner et al., 2010; Weeraratne et al., 2003) models of shear velocity as well as models including azimuthal (Debayle & Ricard, 2013; Li et al., 2003) and radial (Beghein et al., 2014; Moulik & Ekström, 2014) anisotropy. Rayleigh wave phase velocities can also be used in combination with other data types such as Rayleigh wave ellipticity (Gao & Lekić, 2018) and receiver funtions (Eilon et al., 2018) to constrain 1-D velocity structure beneath seismic stations. FM Rayleigh wave amplitudes are essential in studies of upper-mantle seismic attenuation (Bao et al., 2016; Selby & Woodhouse, 2002) and increasingly are used in determining velocity models (Dalton & Ekström, 2006; Forsyth & Li, 2005; Lin & Ritzwoller, 2011).

In addition to the FM surface waves, earthquakes excite higher-mode surface waves, which in a normal-mode framework correspond to free oscillations with radial order $n > 0$. These higher-mode surface waves, or overtones, affect studies of Earth structure in two ways. One, their sensitivity kernels are more complex and sample deeper structure than the kernels for the FM waves, offering potential to image deeper structure such as the transition zone and uppermost lower mantle. Two, the overtones can interfere with the FM when the group arrival windows overlap. This interference can bias measurements of the FM if it is not accounted for. This has been recognized as a problem for Love waves, particularly in oceanic settings where the group velocity curves of different mode branches overlap (Figure 1b).

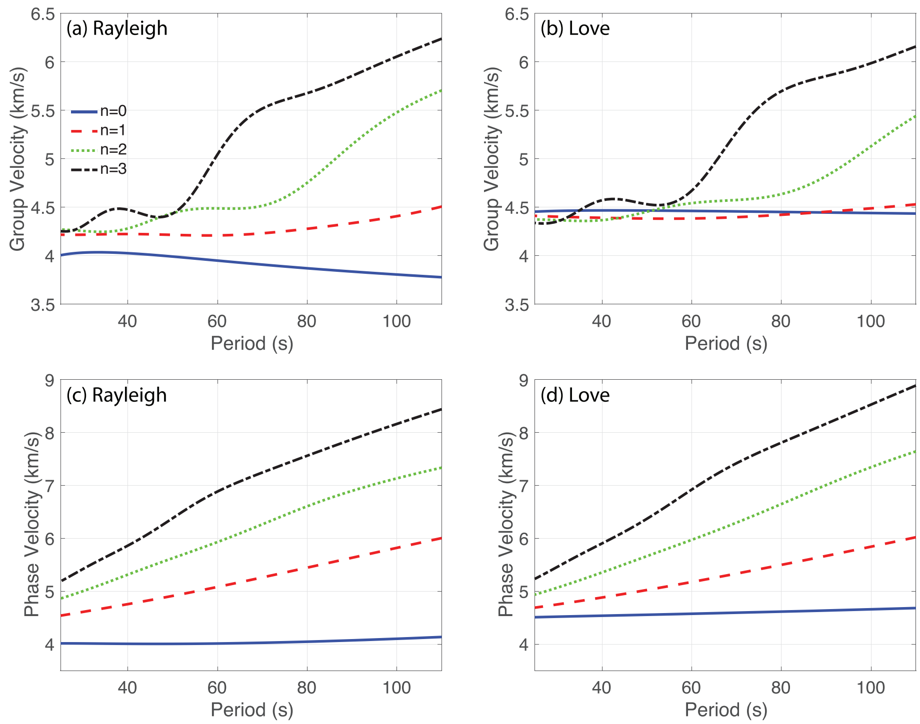

Figure 1. Rayleigh and Love wave group and phase velocity for the fundamental mode (n=0) and the first three higher modes. Group and phase velocities are calculated with MINEOS for the oceanic model ATL2a (James et al., 2014)

Early studies of higher-mode interference for Love waves debated whether the difficulty reconciling FM Rayleigh wave and Love wave phase velocities was due to overtone interference (Thatcher & Brune, 1969) or radially anisotropic seismic structure (Boore, 1969). Forsyth (1975b) showed that both factors mattered. A statistically significant lower misfit to Love wave phase observations was obtained when the phase velocity of the first higher mode was included as an unknown parameter in inversions (Forsyth, 1975a), but accounting for the overtone interference did not eliminate the inconsistency between Rayleigh wave and Love wave data sets (Forsyth, 1975b). More recently, Nettles and Dziewoński (2011) demonstrated, using tests with synthetic and real data, that global long-wavelength patterns of upper-mantle radial anisotropy are not an artifact of overtone interference.

Higher-mode interference does not introduce a systematic bias into global maps of FM Love wave phase velocity because such global inversions include measurements from a wide range of path lengths and because the overall perturbation to the total path-integrated travel time is relatively small. The overlapping group velocities of FM and overtone Love waves cause overlapping group arrival times, but the differing phase velocities (Figure 1d) cause the degree of constructive and destructive interference to vary with path length. By modeling a Love wave arrival as the interference between two sinusoidal waves, the wavelength of the interference pattern can be shown to depend on the phase velocities of the two waves (Foster, Nettles, et al., 2014; Jin, 2015; Thatcher & Brune, 1969). Thus, as long as many paths of sufficiently different lengths are used, the bias in the individual measurements can be suppressed (Boore, 1969; Forsyth, 1975b; Foster, Nettles, et al., 2014; Nettles & Dziewoński, 2011). However, the strong dependence of the Love wave interference pattern on path length introduces significant bias into estimates of Love wave phase velocity between pairs or small groups of nearby stations. Foster, Nettles, et al. (2014) showed that phase-velocity errors can be up to 10% when the two-station method (interstation distance = 350 – 750 km) is used and up to 20% when a mini-array method (interstation distance < 225 km) is used. Moreover, because the shape of the interference pattern with distance is saw-toothed rather than symmetric, the two-station and mini-array methods can introduce an overall bias toward fast phase velocities (Foster, Ekström, et al., 2014; Foster, Nettles, et al., 2014).

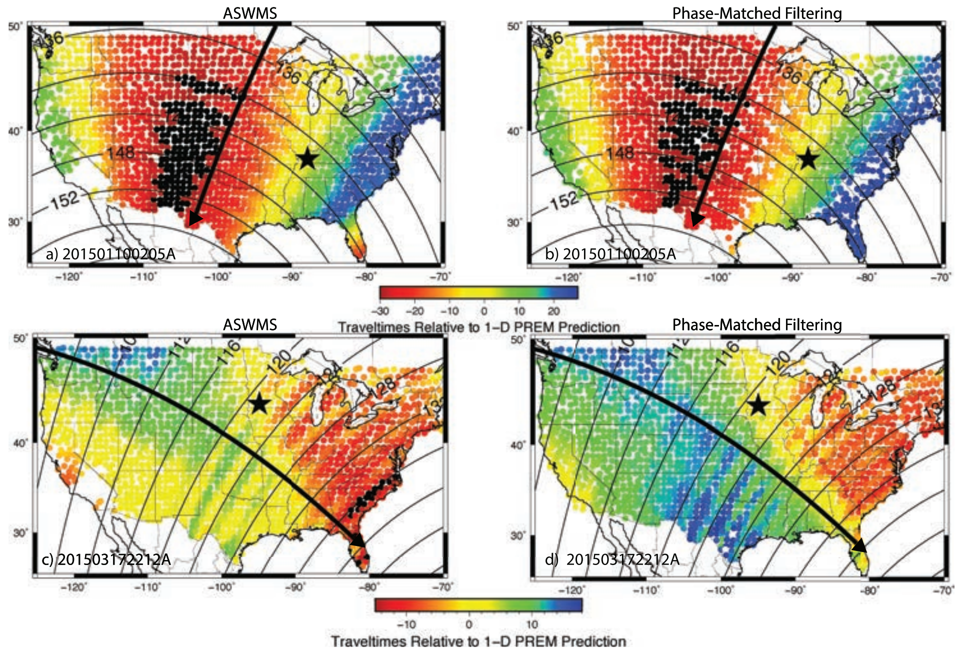

Figure 2. Rayleigh wave travel-time measurements on ShakeMovie synthetic seismograms, at 100 s. Measurements are shown for two events in the Global CMT catalog: 201501100205A (a,b) and 201503172212A (c,d). Event 201501100205A is located at 5.74^{o}W, 68.32^{o}N, and 12-km depth. Event 201503172212A is located at 126.5^{o}E, 1.77^{o}N, and 41.7-km depth. Measurements made with the ASWMS (a,c) and phase-matched filtering (b,d) methods are compared. Travel times predicted with PREM have been subtracted to emphasize the effects of propagation through a heterogeneous Earth model. For ease of comparison, the travel times are plotted relative to a reference station (shown as a black star). The black arrow illustrates a great-circle ray path. Contours of epicentral distance, spaced 4 degrees apart, are overlain and labeled.

Unlike for the Love waves, the group velocities of the FM and higher-mode Rayleigh waves are well separated (Figure 1a). A number of methods have been developed to utilize the overtone signal in seismograms in order to improve seismic imaging of the mantle transition zone. These strategies include array-based methods (Matsuzawa & Yoshizawa, 2019; Nolet, 1975), the use of pure-mode synthetic seismograms (Cara & Lévêque, 1987; van Heijst & Woodhouse, 1997), full-waveform inversion (Bozdag et al., 2016; Li & Romanowicz, 1996; Lebedev & Nolet, 2003; Woodhouse & Dziewonski, 1984), linear Radon transform (Luo et al., 2015), and model-space searches (Visser et al., 2007; Xu & Beghein, 2019; Yoshizawa & Ekström, 2010). Nonetheless, approaches designed to isolate the FM Rayleigh wave take steps to avoid overtone interference. These steps include using only shallow earthquakes, which most strongly excite the fundamental modes, and discarding measurements from paths with epicentral distances $<$ 20 degrees and $>$ 160 degrees to avoid interference between the minor-arc FM and overtones along short paths and between the minor-arc and major-arc FM along long paths (Ekström et al., 1997; Levshin et al., 2005).

Here, we show that the well separated Rayleigh wave group-velocity curves cause minor-arc FM Rayleigh wave measurements to be impacted by interference with higher-mode Rayleigh waves on the major arc (sometimes referred to as *Xn* phases, where *n* is the orbit number of the overtones). Traveling at greater speeds, the higher modes along the major arc arrive in the same time window as the fundamental mode along the minor arc, mostly at distances > 120 degrees for the shallow earthquakes considered in this study. We use synthetic seismograms to characterize the interference. We also show that the interference is present in real data, can affect phase-velocity maps depending on the path lengths used, and results in increased measurement errors for long paths.

2. Data and Methods

The analysis described in sections 3 and 4 utilizes measurements of Rayleigh wave travel time and amplitude. These measurements are made on synthetic waveforms generated by SPECFEM3D_GLOBE and normal-mode summation as well as on observed waveforms at USArray stations. The measurements are

10.1029/2019JB018540

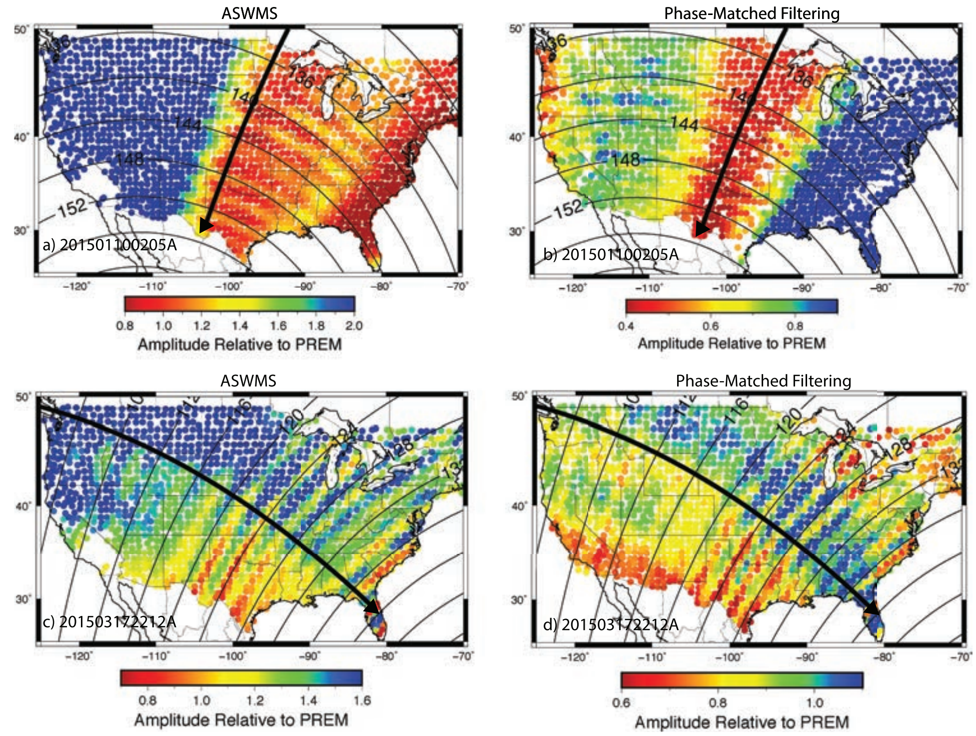

Figure 3. As in Figure 2 but for Rayleigh wave amplitude measurements, also at 100 s. The predicted effects of the source radiation pattern have been removed from the ASWMS measurements. Amplitudes are shown relative to the same reference station for both measurement approaches. Different color scales are used to emphasize the amplitude variations. Contours of epicentral distance, spaced 4 degrees apart, are overlain and labeled.

made using both inter-station and single-station approaches. Finally, phase-velocity maps are generated from the measurements. Below, the details of the data and methods are discussed.

2.1. Synthetic Seismograms

Synthetic seismograms used in this study are generated with two different approaches. To include complex wave-propagation phenomena and the effects of realistic Earth structure, we use seismograms generated from Princeton University's ShakeMovie portal (Tromp et al., 2010) (http://global.shakemovie.princeton.edu, last accessed 7-1-2019), created using the spectral-element code SPECFEM3D_GLOBE and implementing the 3-D Earth model S362ANI (Kustowski et al., 2008), with crustal structure from CRUST2.0 (Bassin et al., 2000).

To perform tests on the influence of different surface-wave overtones in seismograms, we calculate synthetic seismograms using normal-mode summation (Gilbert, 1971) for a known 1-D Earth structure; the mode eigenfunctions and eigenfrequencies are computed with the MINEOS code (Masters et al., 2011). The advantage of mode summation is that we can control which mode branches (i.e., which values of n) are included in the seismograms. Given the prevalence of oceanic paths in global data sets, the 1-D Earth structure used in this study is the oceanic model ATL2A (James et al., 2014), which has a 4 km water layer, a 300 m sediment layer, and a Moho depth of 10.3 km.

The examples shown in sections 3 and 4 utilize a few different earthquake sources. The source parameters for these events are from the Global CMT catalog (Ekström et al., 2012).

2.2. Measurement Approaches

We measure the travel time and amplitude of fundamental-mode Rayleigh waves. We compare measurements made using three different approaches to demonstrate that our results are not dependent on how the measurement is made. The first approach is the Automated Surface-Wave Measurement System (ASWMS) software package (Jin & Gaherty, 2015), which uses multi-channel cross-correlation of waveforms at nearby stations. For each event, single-station travel times are obtained from the inter-station delay times using

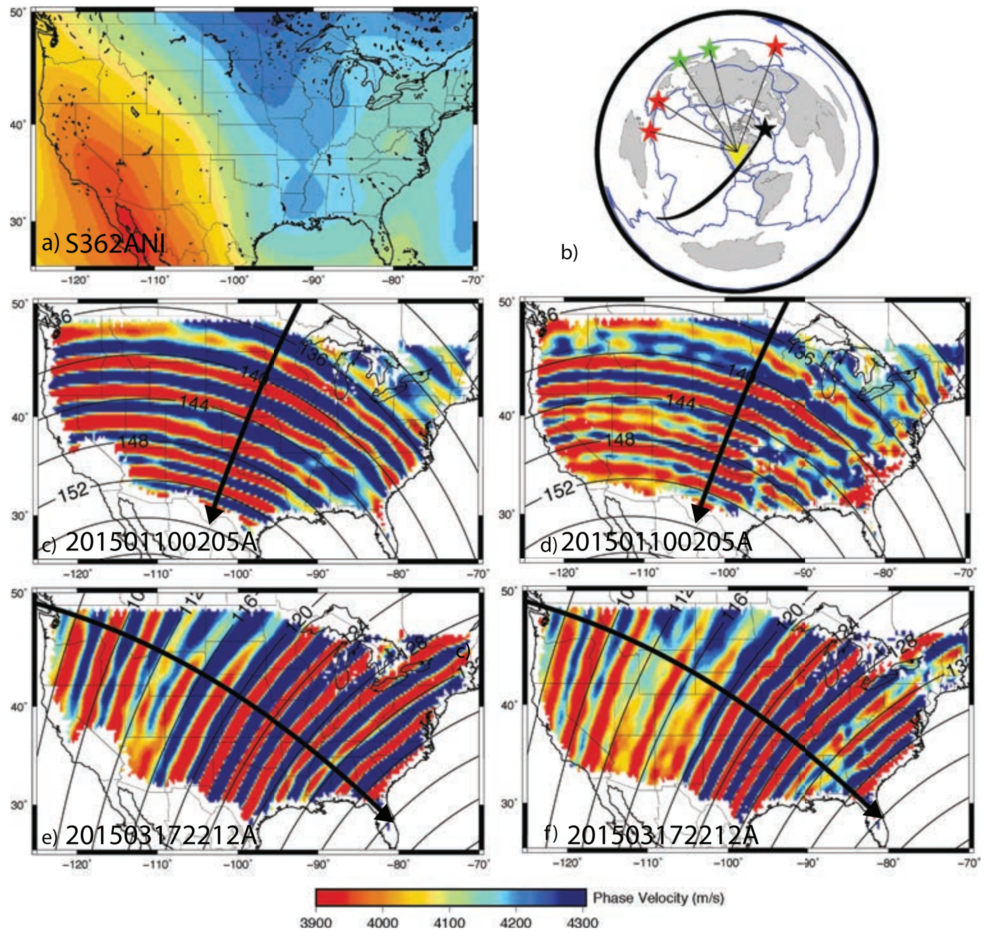

Figure 4. Phase-velocity maps for 100-s Rayleigh waves. (a) Predicted phase velocities for the 3-D model S362ANI with CRUST2.0. Since this model is used to calculate the spectral-element synthetics, this map represents the input structure we expect to recover. (b) Event locations used in this study. Red stars correspond to events with corresponding ShakeMovie synthetics analyzed. Green stars correspond to sources recorded on real data, shown later in the paper (Figure 11). The black star corresponds to a source used in Figures 9 and 10, and the black line shows corresponding stations. (c-f) Event-specific Eikonal phase velocities determined for the same events shown in Figure 2, 201501100205A (c,d) and 201503172212A (e,f), using measurements made with ASWMS (c,e) and phase-matched filtering (d,f). The black arrow illustrates a great-circle ray path. Contours of epicentral distance, spaced 4 degrees apart, are overlain and labeled.

least-squares inversion, and the single-station amplitudes are determined from the square root of the peak of the auto-correlation function of the windowed Rayleigh wave.

The second approach utilizes a phase-matched filter to produce single-station travel-time and amplitude measurements (Ekström et al., 1997). This method, with which the measurements are made relative to synthetic reference seismograms, has been used to generate the phase-delay data sets described by Ekström et al. (1997), Ekström (2011), Foster, Ekström, et al. (2014), Foster, Nettles, et al. (2014) and Eddy et al. (2018). The third approach is the cluster-analysis method of Ma et al. (2014), which relies on time-domain multi-channel cross-correlation to extract the relative travel times. With this method, cluster analysis using cross-correlation as a similarity metric is used to generate clustering trees, from which users can manually eliminate measurements below a desired similarity threshold.

While the focus of this study is synthetic seismograms, we also show some Rayleigh wave travel-time and amplitude measurements made on real data, using the data set of Babikoff and Dalton (2019). These measurements, which exist for the period range 25-180 s, were made using ASWMS (Jin & Gaherty, 2015) on waveforms recorded by 1831 USArray stations. They include 549 earthquakes with $M_w > 6.0$, depth < 50 km, and a maximum epicentral distance of 160 degrees.

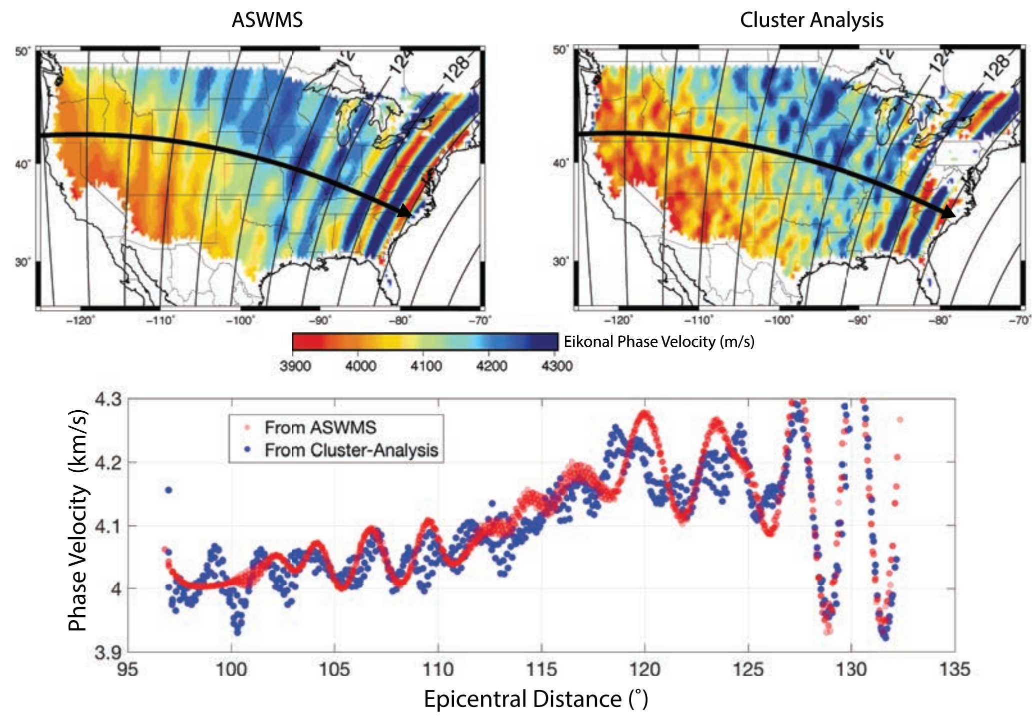

Figure 5. Eikonal phase-velocity maps for 100 s Rayleigh waves. Travel times are measured on ShakeMovie synthetics using ASWMS (left) and the cluster-analysis measurement of Ma et al. (2014) (right) for event 201802251744A, which is located at 142.97^{o}E, 6.29^{o}S, and depth=12 km. The bottom panel shows the along-ray transect through both maps. Contours of epicentral distance, spaced 4 degrees apart, are overlain and labeled.

2.3. Determining Phase Velocity Maps

The phase-velocity maps shown here are generated using either Eikonal tomography (Lin et al., 2009) or Helmholtz tomography (Lin & Ritzwoller, 2011). The governing Helmholtz equation is:

$$\frac{1}{c^2} = |\nabla\tau|^2 - \frac{\nabla^2 A}{\omega^2 A} \tag{1}$$

where τ and A are the measured travel-time and amplitude fields, ω is angular frequency, and c represents the phase-velocity variations to be determined. When the second term on the right-hand side is small, Equation 1 is reduced to the Eikonal equation, and c is determined only from the travel-time field.

In practice, we average the travel-time and amplitude measurements in $0.5^o \times 0.5^o$ cells and interpolate them onto a gridded surface with $0.25^o \times 0.25^o$ cells. Our surfaces are smoothed with a Gaussian filter of width 200 km, and the gradient terms are calculated by finite difference in spherical coordinates. This process is performed separately for each event, and event-specific Eikonal phase-velocity maps are determined from the inverse of $\sqrt{|\nabla\tau|^2}$. To generate composite Eikonal phase-velocity maps from multiple events, we use the median of the $|\nabla\tau|^2$ values in each pixel. For Helmholtz phase-velocity maps we use the median of the entire right-hand side of Equation 1.

3. Results

3.1. Evidence from Spectral-Element Synthetic Seismograms

Our experiments on synthetic seismograms show that Rayleigh wave measurements from certain events exhibit streaks or banding when plotted in map view. Figures 2–4 show examples of 100 s measurements made on ShakeMovie synthetics for two events. Event 201503172212A is a shallow (41.7 km) event in the Northern Molucca Sea, and Event 201501100205A is a shallow (12.0 km) event in the Chagos Archipelago region. The two events are located roughly 120 and 140 degrees from the center of the U.S, respectively. In the maps, bands of alternating advanced and delayed traveltimes (Figure 2), high and low amplitude (Figure 3), and slow and fast velocity (Figure 4) are apparent. In Figure 2, the predicted travel times for propagation in a 1-D Earth model have been subtracted. The orientation of the bands is roughly parallel to wavefronts, and the bands have a similar wavelength in all maps.

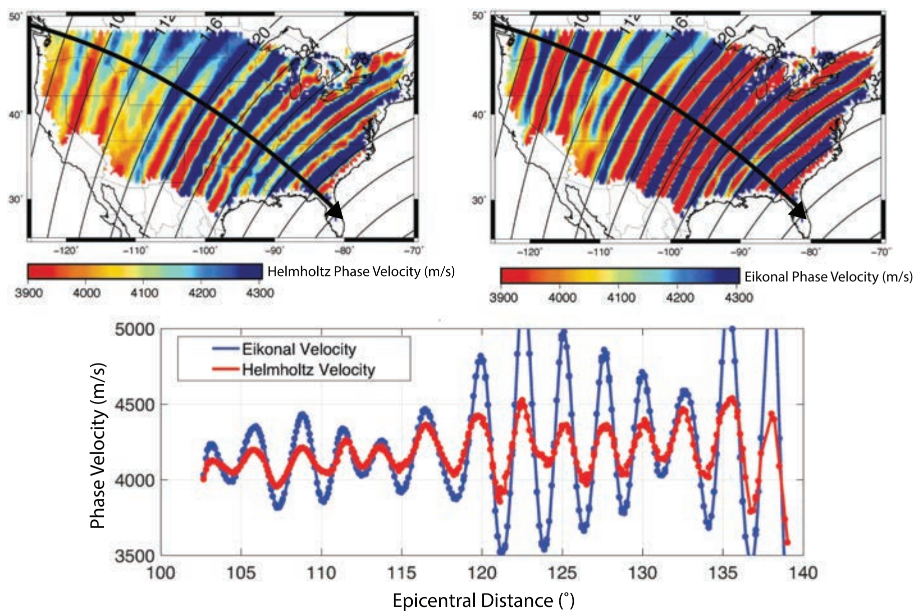

Figure 6. Comparison of Helmholtz and Eikonal phase velocities for 100-s Rayleigh waves for event 201503172212A. Travel times and amplitudes were measured using ASWMS. Left: Helmholtz velocities plotted in map view. Right: Eikonal velocities in map view (as in Figure 4e). Bottom: Transect along ray path comparing Helmholtz (red) and Eikonal (blue) phase velocities. Contours of epicentral distance, spaced 4 degrees apart, are overlain.

The banding is not characteristic of a particular measurement method. With the ASWMS approach, the travel times are derived from inter-station cross-correlation, and with the phase-matched filtering approach, the travel times are single-station measurements made with respect to 1-D synthetic waveforms. Yet the travel times (Figure 2) and the phase-velocity maps determined from them (Figure 4) exhibit the bands for both measurement approaches. The amplitudes are obtained from single-station auto-correlations with ASWMS and relative to a reference synthetic waveform that includes the source radiation pattern, 1-D attenuation, and geometrical spreading with the phase-matched filtering approach. All four examples of the amplitude field (Figure 3) show the oscillatory features. In Figure 5, as an example of a third event and a third measurement approach, we compare Eikonal phase velocities determined from travel times measured with ASWMS and with the cluster-analysis method of (Ma et al., 2014) for a shallow event (12 km) at Papua New Guinea, roughly 115 degrees from the center of the array. The banding is apparent in both sets of measurements from this event, especially at stations located $>$ 120 degrees from the earthquake.

For the events in Figure 4, the streaks obscure the long-wavelength phase-velocity features we expect to recover, whereas the example in Figure 5 more successfully recovers the input structure with the exception of pixels in the eastern U.S., which are located $>$ 120 degrees from the earthquake. An advantage of using the Eikonal equation is that it utilizes only the travel times; the Eikonal phase-velocity maps therefore represent how the anomalies in the travel-time measurements will impact estimates of velocity. Since the streaks are also present in the amplitude measurements, it is reasonable to wonder whether they could be suppressed if the Helmholtz equation (Equation 1) is instead used. By comparing the Eikonal and Helmholtz phase-velocity maps for all events we have analyzed, we have found that this is true to an extent; the amplitude of the banding is weaker, though still significant, in the Helmholtz phase-velocity maps. Figure 6 shows a comparison of Eikonal and Helmholtz velocities in map view and along a transect for event 201503172212A measured with ASWMS. The inability of the Helmholtz equation (Equation 1) to fully account for the interference is likely because the assumption that the interfering waves have the same phase velocity is violated.

Figures 5 and 7 show along-ray transects of amplitude and Eikonal phase velocity, measured with different methods, as a function of epicentral distance. These figures highlight the agreement between measurements made with different approaches. They also show the approximate wavelength of the bands ($\approx 3-5$ degrees, depending on location) and suggest that the banding becomes stronger at epicentral distances $>$ 120 degrees. The offset between amplitudes measured with the two different approaches (Figures 7b,d) may be

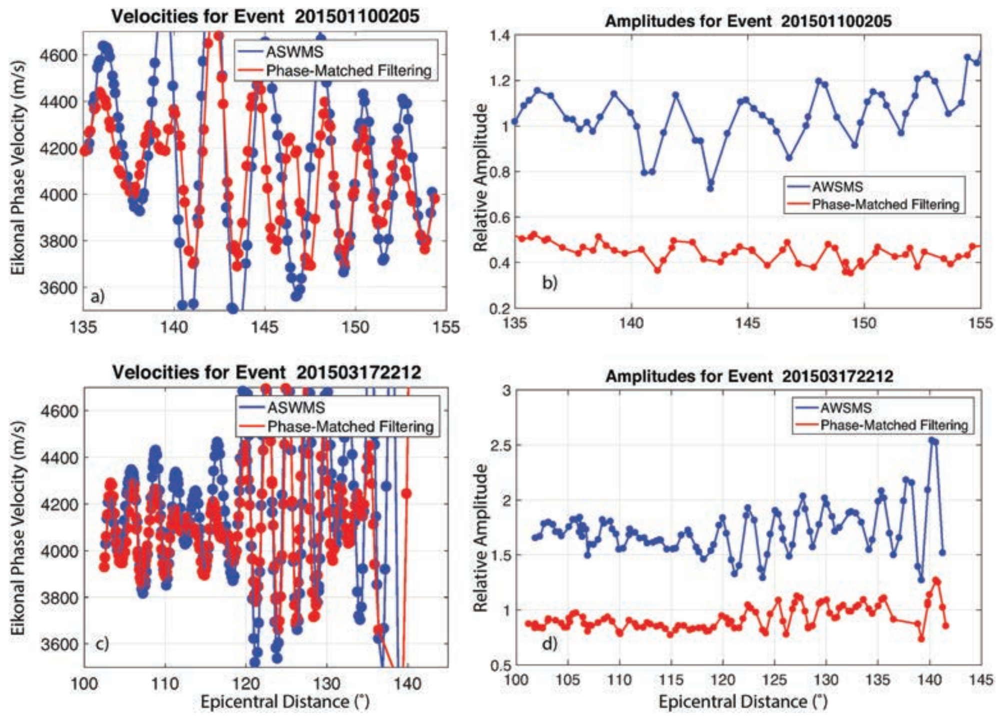

Figure 7. Along-ray transects of Eikonal phase velocity (a,c) and Rayleigh wave amplitude (b,d) for the measurements and phase-velocity maps in Figures 3 and 4. While the transects sample an evenly spaced grid for the phase-velocity maps, they sample USArray station locations for the amplitudes, which explains the difference in sampling density between the two sets of transects.

because the amplitudes measured with the phase-matched filtering approach have had 1-D attenuation and geometrical spreading removed.

3.2. Tests with Normal-Mode Synthetic Seismograms

To explore explanations for the anomalies described in the previous section, we simulate seismograms for the same two events considered in Figures 2-4 using normal-mode summation with the 1-D Earth model ATL2a (James et al., 2014). Two sets of normal-mode seismograms are generated. The first set contains only the fundamental spheroidal modes, and the second set contains the full catalog of spheroidal modes. The summation includes all modes with frequency < 50 mHz and angular order < 500. We use ASWMS to measure Rayleigh wave travel times and amplitudes for the two events. Figure 8 shows the resulting 100 s Eikonal phase-velocity maps. Maps corresponding to synthetic seismograms that contain only the fundamental modes successfully recover the homogenous input phase velocity (Figures 8b,d), but maps corresponding to seismograms containing the full mode catalog do not (Figures 8a,c). These maps contain strong bands of alternating slow and fast velocity. These bands are similar to the ones in Figures 4c,e, suggesting a common mechanism. Moreover, the absence of the bands when only the fundamental modes are used suggests that the interference of the higher modes with the fundamental mode causes the banding. The edge effect seen along the East Coast in Figures 8a,b is due to erroneous travel-time measurements, which result from the relative paucity of stations for which interstation cross-correlation can be conducted.

Record sections of vertical-component synthetic seismograms illustrate the likely explanation (Figure 9a). Normal-mode summation is used to calculate these seismograms for the ATL2a model and event 201502131859A, a shallow (depth=25.2 km) strike-slip event on the Reykjanes Ridge. Stations are evenly spaced along a great-circle path spanning epicentral distances 20-175 degrees. Synthetic seismograms containing only the fundamental mode and containing only higher modes are plotted separately, with the latter amplitude exaggerated by a factor of five. At distances greater than roughly 25 degrees the minor-arc higher-mode Rayleigh waves arrive much earlier than the minor-arc fundamental-mode Rayleigh waves as a result of their distinct group velocities (Figure 1a; Figure 9b). However, at distances $>\approx$ 120 degrees, the major-arc higher-mode Rayleigh waves ($X2$ phases) arrive within the same window as the minor-arc fundamental mode. We suggest that this interference introduces bias into the Rayleigh wave amplitude

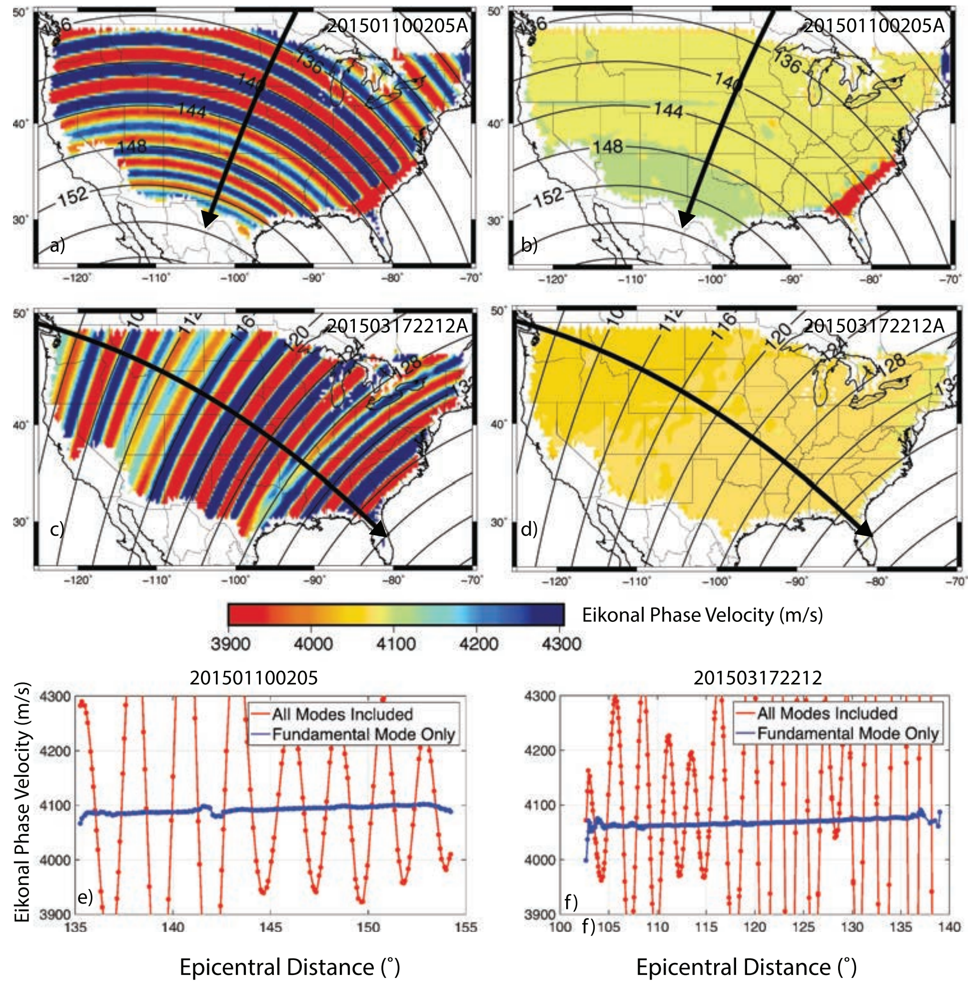

Figure 8. Eikonal phase velocity for 100-s Rayleigh waves for events 201501100205A (panels a, b, e) and 201503172212A (panels c, d, f). The travel times are measured from synthetic seismograms generated with normal-mode summation, using the full mode catalog (a,c) and only the fundamental modes (b,d). The black arrow illustrates a great-circle ray path. Contours of epicentral distance, spaced 4 degrees apart, are overlain.

and travel-time measurements as the different wavepackets constructively and destructively interfere with each other.

Figure 10 quantifies this interference by measuring the impact on amplitude and travel time for the synthetics in Figure 9. The amplitude and travel time measured from the normal-mode synthetics that contain the full mode catalog are expressed relative to their values measured from the synthetics containing only the fundamental mode. In doing so the effects of the source radiation pattern, attenuation, and geometrical spreading will be cancelled out, allowing the effects of higher-mode interference to be isolated. These comparisons show a slight and long-wavelength perturbation to amplitude and travel time at distances < 50 degrees, presumably due to interference between the minor-arc fundamental and higher modes (Figure 9), and larger and shorter-wavelength perturbations at distances > 120 degrees. These short-wavelength perturbations are largest around 140 degrees, where branches 2 and 3 overlap with branch 0.

Foster, Nettles, et al. (2014) calculated the interference of higher-mode Love waves with the fundamental-mode Love waves. It differs from the Rayleigh wave higher-mode interference patterns in Figure 10 in several aspects. One, the Love wave interference pattern is present throughout a broad range of epicentral distances, in contrast to the Rayleigh wave pattern, which is most prominent at distances > 120 degrees. Two, the perturbations that characterize the Love wave interference pattern are relatively constant across a broad distance range, whereas the Rayleigh wave perturbations are strongly dependent on

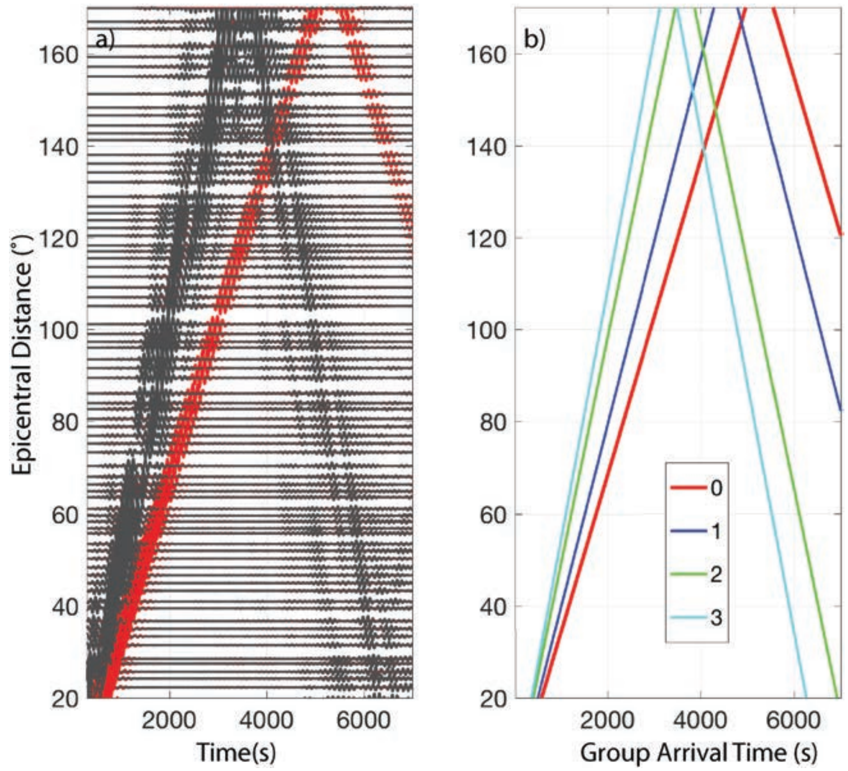

Figure 9. (a) Record sections of vertical-component synthetic seismograms calculated using normal-mode summation for event 201502131859A. Event 201502131859A is located at 32.74^{o}W, 52.7^{o}N, and 25.2-km depth. Two sets of seismograms are shown, bandpass-filtered with a center period at 100 s. The red traces contain only the fundamental mode, and the black traces contain all mode branches except the fundamental mode; for easier visualization the black traces are vertically exaggerated by a factor of 5. (b) Predicted group arrival times for the first four mode branches as a function of epicentral distance using ATL2a-predicted group velocities for period = 100 s.

distance. Three, the Love wave interference pattern has a longer wavelength ($\approx$ 20 degrees), in contrast to the $\approx$ 3-degree wavelength of the Rayleigh wave pattern at distances > 120 degrees.

These differences can be understood from the Rayleigh and Love group and phase velocities (Figure 1). For Love waves, the overlapping group velocities cause the minor-arc fundamental and higher modes to interfere across a broad range of distances, whereas the well separated Rayleigh wave group velocities cause the higher modes to pass into and out of the fundamental-mode window. The wavelength of the interference pattern is dictated by the relative phase velocities of the interfering modes (Foster, Nettles, et al., 2014; Thatcher & Brune, 1969), with a larger difference causing a shorter-wavelength pattern. Although the relative phase velocities between modes are not dramatically different for the Rayleigh waves and Love waves, major-arc higher modes are traveling in the opposite direction from the minor-arc fundamental mode. Thus, the relative phase velocity will appear much larger; for Rayleigh wave branches 2 (c=7.1 km/s) and 0 (c=4.1 km/s), the difference will appear to be 11.2 km/s rather than 3.0 km/s. This can explain the short-wavelength nature of the Rayleigh wave interference pattern.

3.3. Interference in Real Data

Because the higher-mode interference pattern is characterized by short wavelengths and is strongest at epicentral distances > 120 degrees, it will be easiest to observe in real data with long arrays of densely spaced stations. Furthermore, real data will be noisier and have greater wavefield complexity than the rather idealized synthetic seismograms analyzed in Sections 3.1-3.2. Nonetheless, using Rayleigh waves recorded by the EarthScope USArray stations for events with ray paths traveling along the long axis of the Transportable Array deployment, we have found travel-time and amplitude anomalies that are similar to those observed in the synthetic data. Figure 11 shows the Eikonal velocities and amplitudes for two events; these travel-time and amplitude data are from the study of Babikoff and Dalton (2019), in which Rayleigh waves were measured using ASWMS for 549 events in the period range 25-180 s. The real data exhibit oscillations in velocity

10.1029/2019JB018540

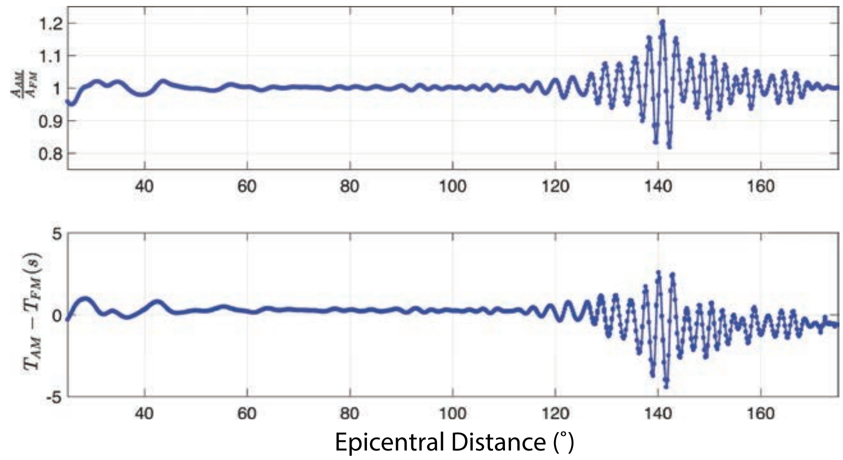

Figure 10. Rayleigh wave amplitudes (top) and travel times (bottom) measured at 100 s using ASWMS for the synthetics in Figure 9. The measurements from synthetics containing the full mode catalog (AM) are plotted relative to those from synthetics containing only the fundamental mode (FM).

and amplitude along a ray path. Both the wavelength and the magnitude of the oscillations in the real data are similar to those present in the measurements made on synthetic data, suggesting that the anomalies are generated by interference of the higher-mode major-arc Rayleigh wave with the minor-arc fundamental mode. In Section 4 we consider how this interference affects Rayleigh wave phase-velocity maps on regional and global scales.

4. Discussion

4.1. Implications for USArray Measurements & Phase Velocity Maps

In this section we evaluate the effects of the overtone interference on the 100-s Rayleigh wave travel-time measurements made at USArray stations in the contiguous U.S. by Babikoff and Dalton (2019) and on the Eikonal phase-velocity maps determined from that data set. The effects of overtone interference (i.e., the oscillations with distance) are not visible in the single-station travel-time measurements, mostly because the dominant signal is from 3-D structural heterogeneity. We predict and remove the long-wavelength velocity variations from the travel-time data by integrating along the great-circle path through GDM52, the global phase-velocity maps of Ekström (2011). Since the predictions are path-integrated travel times and the measurements of Babikoff and Dalton (2019) are expressed relative to the travel time at a reference station, we convert the measurements into path-integrated times by fixing the travel time at the reference station to the predicted value and applying this static offset to all other relative travel times. For 90% of the 208,233 paths from Babikoff and Dalton (2019) the path-averaged phase-velocity anomaly is within 0.5% of the GDM52 predictions. Figure 12a shows the median absolute velocity difference in one-degree epicentral distance bins; all bins between 17 degrees and 152 degrees contain at least 200 paths. The calculation shows that paths in the distance range 70-120 degrees are fit best by the GDM predictions, with higher residuals at distances < 70 degrees and > 120 degrees. Comparison of Figures 12a and the bottom panel of Figure 10 suggests that the elevated residuals at distances > 120 degrees correspond to interference with the major-arc higher modes; we speculate that the signal for short paths may be due to interference with the minor-arc higher modes (Figure 9).

With Eikonal and Helmholtz tomography (Lin et al., 2009; Lin & Ritzwoller, 2011) individual phase-velocity maps are generated for each event, and then they are combined to yield a single composite phase-velocity map at a given period. Figure 12b shows the median absolute difference between the event-specific Eikonal phase-velocity maps and the portion of the global GDM52 map confined to the contiguous U.S. For this figure distance is calculated from the center of each $0.25^o \times 0.25^o$ pixel and the corresponding earthquake location. This calculation makes use of event-specific velocities from 549 earthquakes and a total of 11,932 pixels, although most of the event-specific phase-velocity maps consist of roughly 2100 pixels. The median residual phase velocity is $\approx$ 100 m/s (2%) at distances $<$ 120 degrees; the residual peaks at distance $\approx$ 140 degrees, where it is 422 m/s (10%).

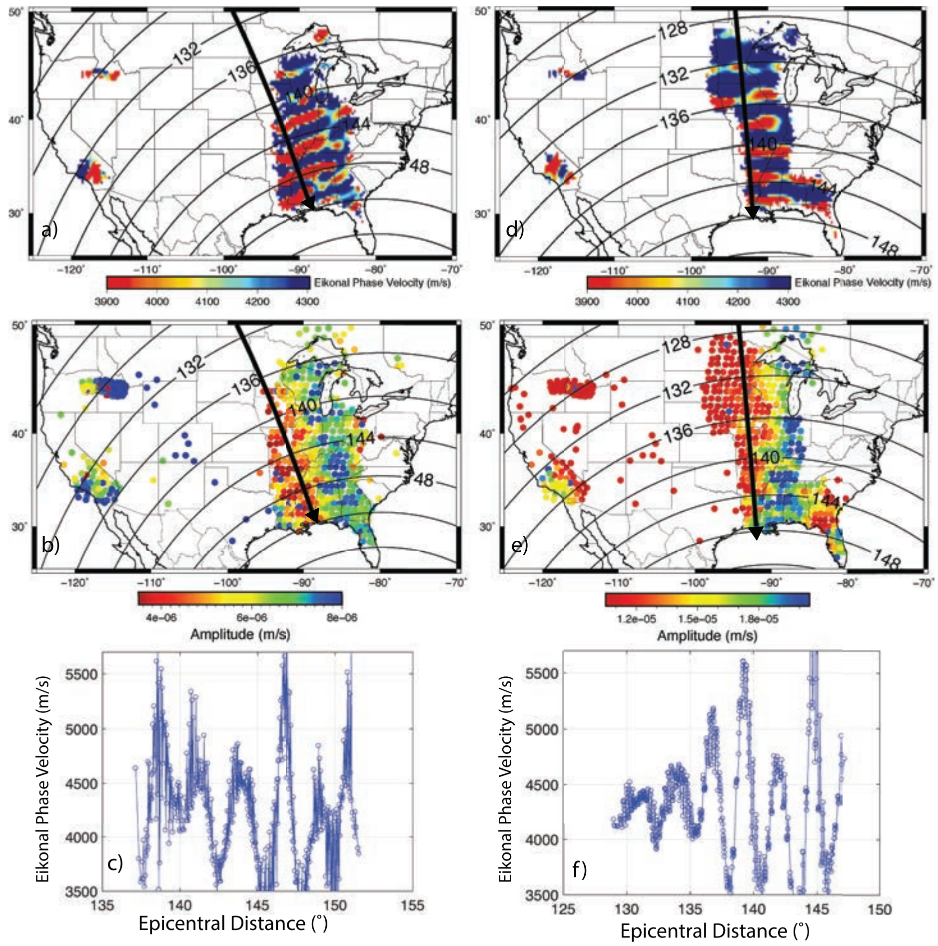

Figure 11. Evidence of the interference in real data using the 100-s Rayleigh wave travel-time and amplitude measurements from Babikoff and Dalton (2019) for two events, 201204150557 (a-c) and 201209140451 (d-f). Event 201204150557 is located at 90.31^{o}E, 2.49^{o}N, and 33.0-km depth. Event 201209140451 is located at 100.32^{o}E, 3.58^{o}S, and 12.0-km depth. These measurements were made using ASWMS. Eikonal velocities determined from the travel times are shown in map view (a,d) and as transects (c,f), and amplitudes are shown in map view (b,e). The black arrow illustrates a great-circle ray path. Contours of epicentral distance, spaced 4 degrees apart, are overlain.

Figure 12b makes clear that the event-specific phase velocities for distances > 120 degrees are characterized by large errors. In Figure 13 we explore how the composite map is affected when velocities that may be biased by the higher-mode interference are excluded. Referring to Equation 1, the composite Eikonal maps are generated from the inverse of the square root of the median of all $|\nabla\tau|^2$ values in each pixel. In Figure 13b we only include an event-specific $|\nabla\tau|^2$ value in the median calculation if the distance between the earthquake and pixel is < 115 degrees, and in Figure 13c only $|\nabla\tau|^2$ values from earthquakes > 115 degrees are included. For this test we use the Rayleigh wave Eikonal maps of Babikoff and Dalton (2019). Figure 13d shows that the number of distant events (> 115 degrees) is much smaller than the number of nearby events (< 115 degrees). Since the median value may not be as robust if determined from a small number of measurements, we require that the number of distant and nearby events used at each pixel is the same. In practice, in each pixel we randomly select a subset of the nearby events; this results in a speckled appearance of the map in Figure 13b. Because most pixels are dominated by data from events at distances < 115 degrees, the similarity between Figures 13a and 13b shows that the composite map generated from all data is not biased by the inclusion of data from events at distances > 115 degrees. However, Figure 13c illustrates the potential pitfalls of including data biased by interference effects; this composite map differs significantly from the composite map determined from all data. As mentioned earlier, the impact of this interference is somewhat weaker for maps constructed using Helmholtz tomography (Figure 6).

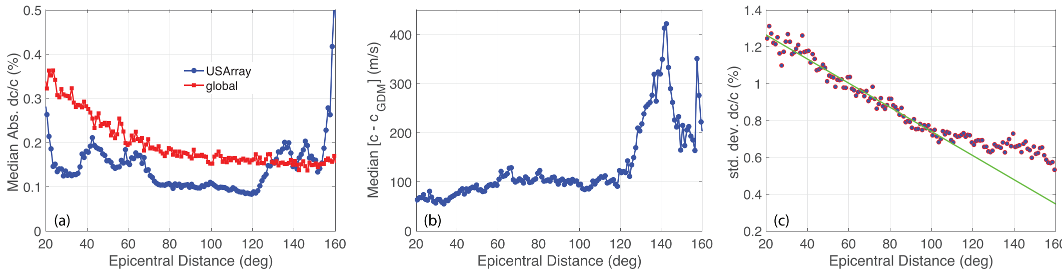

Figure 12. Evidence of higher-mode interference in USArray and global data sets of 100-s Rayleigh wave travel times and phase velocities. (a) The median absolute difference of the path-averaged phase-velocity anomalies (dc/c), binned by epicentral distance. Path-averaged dc/c predicted by integrating through the GDM52 phase-velocity map is subtracted from the measured values. Results are shown for 208,233 measurements at USArray stations (Babikoff & Dalton, 2019) and 282,996 measurements at global stations (Ekström, 2011). (b) Median absolute phase-velocity difference (m/s) in the contiguous U.S. between 549 event-specific Eikonal maps of Babikoff and Dalton (2019) and the U.S. portion of the GDM52 global map. (c) Standard deviation of the path-averaged phase-velocity anomalies in the global data set of Ekström (2011), binned by epicentral distance. Green line shows linear regression applied to values in the distance range 20-110 degrees.

4.2. Implications for Global Rayleigh Wave Data Sets

To investigate the possible impact of Rayleigh wave higher-mode interference on global studies, in Figure 12a we plot the median residual path-averaged phase-velocity anomaly determined from the global 100-s phase-delay data set of Ekström (2011). As with the analogous USArray calculation, the measured anomalies are expressed relative to predictions obtained from integrating the GDM52 global map along the great-circle path. In general the median residuals are comparable in size to the USArray residuals ($\approx 0.2\%$). However, unlike the USArray residuals, the global data set does not show evidence of a larger mismatch between observations and predictions for path length $>$ 120 degrees as might be expected for major-arc higher-mode interference. On the other hand, Figure 12c hints at larger errors in the global data set for paths longer than 120 degrees. It shows the standard deviation of all measurements in each one-degree distance bin. All bins in the distance range 20-160 degrees contain at least 500 measurements, and this calculation utilizes measurements that have not been corrected for propagation through the GDM52 map. The data reveal a linear decline in standard deviation with distance for path lengths $<$ 110 degrees. A larger spread in measurements for shorter paths is expected, since they can be confined to regions with relatively uniform seismic properties– for example, some short paths will travel only through continents whereas others will travel only through oceans. Long paths necessarily integrate across a range of tectonic settings, which will tend to homogenize the path-averaged phase velocities. The linear decline is interrupted for path lengths $>$ 110 degrees. This may indicate larger uncertainties in these measurements due to higher-mode interference.

Since our results suggest that interference varies as a function of path length, we explore the question of whether measurements made at different locations on Earth are more prone to interference, as the distribution of path lengths sampled at any position on the Earth varies due to the global distribution of earthquake sources. Figure 14a shows the proportion of events with path lengths $>$ 115 degrees. The 971 earthquakes used for this calculation are from the Global CMT catalog (Dziewonski et al., 1981; Ekström et al., 2012) for the years 2013, 2014 and 2015 with $M_w > 5.5$ and depth $<$ 70 km. For a hypothetical station located along the southern Mid-Atlantic Ridge, roughly 50% of the shallow earthquakes it records will be located $>$ 115 degrees away, and we predict that measurements of the minor-arc Rayleigh waves will therefore be more susceptible to higher-mode interference. Plans for future deployments of ocean-bottom seismometers may want to take this into consideration. Figure 14a also shows, however, that most regions of the Earth are not dominated by long paths, and thus Rayleigh wave measurements in those regions will experience only a nominal impact from interference bias. Figure 14b shows that global Rayleigh wave data sets do contain these regional variations in path length to earthquakes. We calculate epicentral distance for each event-station pair in the data set of Ekström (2011) and determine the fraction of events located $>$ 115 degrees away from each station. Figure 14b shows that for stations located along the western edge of the Atlantic basin, roughly 50% of the measurements could be prone to interference.

Overall we expect that regional and global phase-velocity maps will be minimally affected by the higher-mode interference. First, most data sets are dominated by path lengths $<$ 120 degrees. In addition,

10.1029/2019JB018540

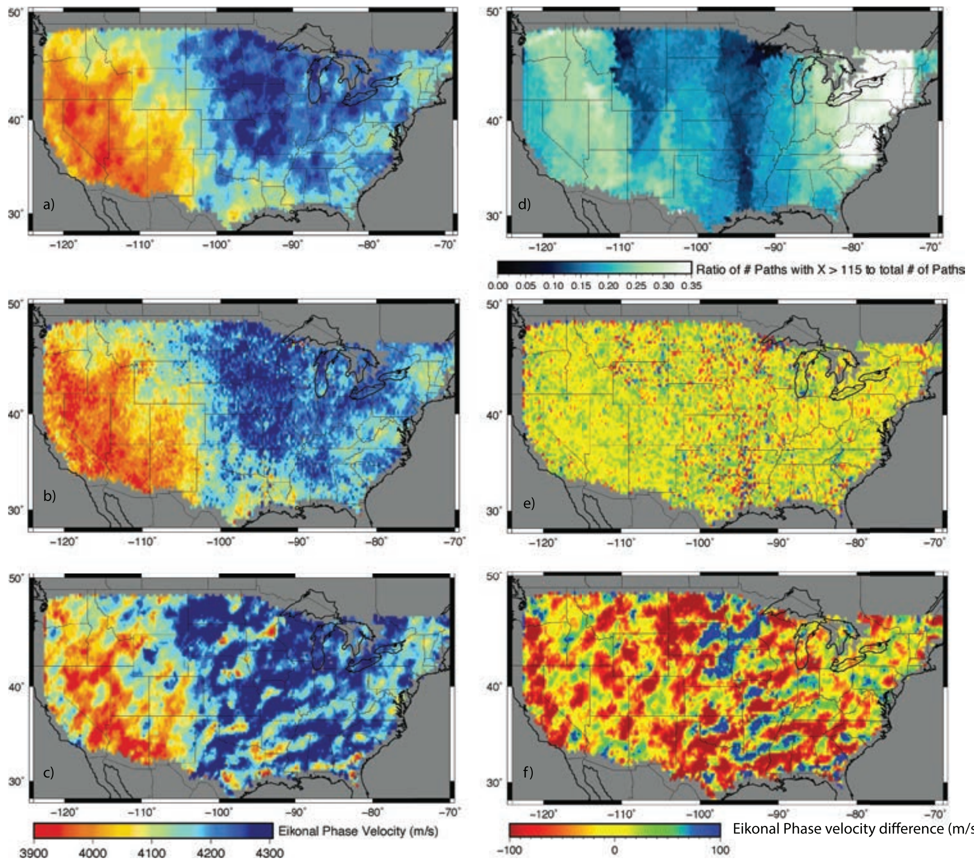

Figure 13. Eikonal phase velocities for 100 s Rayleigh waves calculated from the database of Babikoff and Dalton (2019) for measurements grouped into different subsets based on path length. (a) All measurements are used. (b) Only measurements with path lengths < 115 degrees are used. (c) Only measurements with path lengths > 115 degrees are used. (d) Hit count map showing proportion of all measurements with path lengths > 115 degrees. (e) Difference between panels (b) and (a). (f) Difference between panels (c) and (a).

the fact that the oscillations vary with distance and have a short wavelength means that systematic bias is unlikely to result given a large number of measurements. Second, for phase-velocity inversions that use path-integrated travel times as data, the ± 5 second perturbation introduced by higher-mode interference (Figures 2 and 10) will not result in a large bias in inverted phase velocity. Damping and smoothing, which are traditionally applied to these inversions, will help to suppress any streaks or banding. On the other hand,

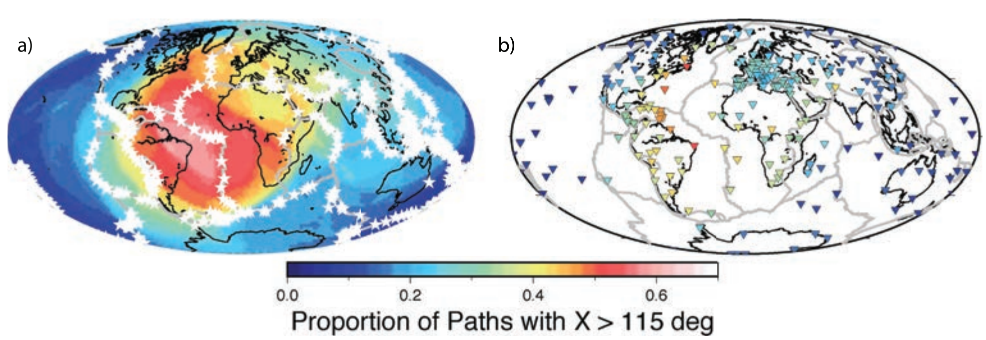

Figure 14. (a) Map view showing, in each pixel, the number of events located > 115 degrees away from each pixel, plotted as a fraction of the total number of events considered in the calculation. White stars show earthquakes used in the calculation, which are from the Global CMT catalog with depth < 70 km and $M_w \geq 5.5$ for the years 2013-2015. Tectonic plate boundaries from Bird (2003) are overlain. (b) As in (a), but calculated using only the source-station event pairs used in the construction of the GDM52 model at 100 s for Rayleigh waves (Ekström, 2011)

phase-velocity inversions based on travel-time differences between pairs or small groups of nearby stations (Foster, Ekström, et al., 2014; Lin et al., 2009) are more susceptible to bias from higher-mode interference.

Furthermore, travel-time and amplitude measurements that are strongly biased by the interference may be removed as part of quality control procedures, a notion discussed by Thatcher and Brune (1969) in the context of Love wave interference. An additional consideration is that measurements of fundamental-mode Rayleigh waves on the major arc (R2) may be biased by interference with higher modes traveling on the minor arc after completing one orbit (often termed $X3$ phases), and the group velocities in Figure 1a suggest that the interference for R2 will occur over a much wider range of epicentral distances ($\approx$ 20 − 90 degrees) than the minor-arc interference considered here. Finally, we note that our study has used 100 s Rayleigh waves to document the phenomenon of higher-mode interference and describe its general characteristics. Measurements made at other periods also show evidence of the interference. In both Eikonal velocity (Figure S1) and amplitude (Figure S2), it is clear that the wavelength of the interference pattern decreases with decreasing period and that the onset of the strongest interference is consistently around 120 degrees.

Future work will investigate how the earthquake source, including its moment tensor and depth, the velocity structure, and the period affect the characteristics of higher-mode interference. Major-arc overtone interference also holds the potential for studies to image higher-mode wave propagation through a unique lens, as the interference signal preserves information about the phase velocity and amplitude of the higher modes while the large distance range of the major-arc phase ensures the individual mode branches are well separated in time. Previous studies (Forsyth, 1975b; Thatcher & Brune, 1969) have demonstrated the potential to model the relative amplitude and phase velocity of individual modes in a travelling-wave signal using the superposition of plane waves, suggesting that the same principle can be applied to the wavefield identified here. The ability to extract information about overtone phase velocity and amplitude would allow new investigations in the velocity and attenuation structure of the mantle transition zone and uppermost lower mantle.

5. Conclusion

We show that interference of Rayleigh wave major-arc overtones with the minor-arc fundamental mode can be detected in travel-time and amplitude measurements made on synthetic and real waveforms. This interference manifests as oscillations about the underlying value along a ray path. Comparing synthetic seismograms computed by normal-mode summation with a full mode catalog and with only the fundamental modes shows that the higher modes traveling along the major arc overlap with the fundamental mode along the minor arc, thus producing the interference. The interference is most pronounced for relatively long paths (epicentral distance > 120 degrees) and is characterized by a wavelength of $\approx$ 3 degrees at 100 s.

The interference is most easily observed with dense arrays of seismometers, and we have found examples of it in real data recorded by the EarthScope USArray stations. The impact of the interference on estimates of Rayleigh wave phase velocity will be larger for approaches based on relative travel times between stations than for approaches that use path-integrated travel times, such as most global studies. Overall, we expect that the impact of the interference will be small since most data sets are dominated by measurements from path lengths < 120 degrees. We show that, as a consequence of the global distribution of earthquakes, measurements made at stations in and around the Atlantic Ocean are more susceptible to interference bias. Looking forward, modeling various characteristics of the interference pattern, including its distance dependence, wavelength, and amplitude, may allow the phase and group velocities and amplitudes of higher-mode Rayleigh waves to be measured.

Acknowledgments
The authors thank Kazunori Yoshizawa and Ge Jin for helpful and constructive suggestions and reviews that improved the quality of this manuscript. We also thank Don Forsyth and others in the Brown University Seismology and Geophysics Groups for helpful discussions and suggestions, and acknowledge useful correspondence with Pritwiraj Moulik. Some figures were made using the generic mapping tools (Wessel and Smith, 1998). We also thank the group at Princeton University maintaining the ShakeMovie Portal for making synthetic seismograms accessible. A.H. was supported by a NSF Graduate Research Fellowship under grant 1644760. This work has been funded by NSF grant EAR-1553367 to C.A.D. Seismograms recorded at USArray stations can be downloaded from the IRIS DMC.

References

Babikoff, J. C., & Dalton, C. A. (2019). Long period Rayleigh wave phase velocity tomography using usarray. *Geochemistry, Geophysics, Geosystems*, *20*, 1990–2006. https://doi.org/10.1029/2018GC008073

Bao, X., Dalton, C. A., & Ritsema, J. (2016). Effects of elastic focusing on global models of Rayleigh wave attenuation. *Geophysical Supplements to the Monthly Notices of the Royal Astronomical Society*, *207*(2), 1062–1079.

Bassin, C., Laske, G., & Masters, G. (2000). The current limits of resolution for surface wave tomography in North America. *Eos*, *81*.

Beghein, C., Yuan, K., Schmerr, N., & Xing, Z. (2014). Changes in seismic anisotropy shed light on the nature of the Gutenberg discontinuity. *Science*, *343*(6176), 1237–1240.

Bird, P. (2003). An updated digital model of plate boundaries. *Geochemistry, Geophysics, Geosystems*, *4*(3), 1027. https://doi.org/10.1029/2001GC000252

Boore, D. M. (1969). Effect of higher mode contamination on measured Love wave phase velocities. *Journal of Geophysical Research*, *74*(27), 6612–6616.

Bozdag, E., Peter, D., Lefebvre, M., Komatitsch, D., Tromp, J., Hill, J., et al. (2016). Global adjoint tomography: First-generation model. *Geophysical Journal International*, *207*(3), 1739–1766.

Cara, M., & Lévêque, J. (1987). Waveform inversion using secondary observables. *Geophysical Research Letters*, *14*(10), 1046–1049.

Dalton, C., & Ekström, G. (2006). Constraints on global maps of phase velocity from surface-wave amplitudes. *Geophysical Journal International*, *167*(2), 820–826.

Debayle, E., & Ricard, Y. (2013). Seismic observations of large-scale deformation at the bottom of fast-moving plates. *Earth and Planetary Science Letters*, *376*, 165–177.

Dziewonski, A., Chou, T.-A., & Woodhouse, J. (1981). Determination of earthquake source parameters from waveform data for studies of global and regional seismicity. *Journal of Geophysical Research*, *86*(B4), 2825–2852.

Eddy, C. L., Ekström, G., Nettles, M., & Gaherty, J. B. (2018). Age dependence and anisotropy of surface-wave phase velocities in the Pacific. *Geophysical Journal International*, *216*(1), 640–658.

Eilon, Z., Fischer, K. M., & Dalton, C. A. (2018). An adaptive Bayesian inversion for upper-mantle structure using surface waves and scattered body waves. *Geophysical Journal International*, *214*(1), 232–253.

Ekström, G. (2011). A global model of love and Rayleigh surface wave dispersion and anisotropy, 25-250 s. *Geophysical Journal International*, *187*(3), 1668–1686.

Ekström, G., Nettles, M., & Dziewoński, A. (2012). The global cmt project 2004–2010: Centroid-moment tensors for 13,017 earthquakes. *Physics of the Earth and Planetary Interiors*, *200*, 1–9.

Ekström, G., Tromp, J., & Larson, E. W. (1997). Measurements and global models of surface wave propagation. *Journal of Geophysical Research*, *102*(B4), 8137–8157.

Forsyth, D. W. (1975a). The early structural evolution and anisotropy of the oceanic upper mantle. *Geophysical Journal International*, *43*(1), 103–162.

Forsyth, D. W. (1975b). A new method for the analysis of multi-mode surface-wave dispersion: Application to Love-wave propagation in the east pacific. *Bulletin of the Seismological Society of America*, *65*(2), 323–342.

Forsyth, D. W., & Li, A. (2005). Array analysis of two-dimensional variations in surface wave phase velocity and azimuthal anisotropy in the presence of multipathing interference. *Seismic Earth: Array Analysis of Broadband Seismograms*, *157*, 81–97.

Foster, A., Ekström, G., & Nettles, M. (2014). Surface wave phase velocities of the western United States from a two-station method. *Geophysical Journal International*, *196*(2), 1189–1206.

Foster, A., Nettles, M., & Ekström, G. (2014). Overtone interference in array-based Love-wave phase measurements. *Bulletin of the Seismological Society of America*, *104*(5), 2266–2277.

Gao, C., & Lekić, V. (2018). Consequences of parametrization choices in surface wave inversion: Insights from transdimensional Bayesian methods. *Geophysical Journal International*, *215*(2), 1037–1063.

Gilbert, F. (1971). Excitation of the normal modes of the earth by earthquake sources. *Geophysical Journal International*, *22*(2), 223–226.

Hamada, K., & Yoshizawa, K. (2015). Interstation phase speed and amplitude measurements of surface waves with nonlinear waveform fitting: Application to usarray. *Geophysical Journal International*, *202*(3), 1463–1482.

van Heijst, H. J., & Woodhouse, J. (1997). Measuring surface-wave overtone phase velocities using a mode-branch stripping technique. *Geophysical Journal International*, *131*(2), 209–230.

James, E. K., Dalton, C. A., & Gaherty, J. B. (2014). Rayleigh wave phase velocities in the atlantic upper mantle. *Geochemistry, Geophysics, Geosystems*, *15*, 4305–4324. https://doi.org/10.1002/2014GC005518

Jin, G. (2015). Surface-wave analysis and its application to determining crustal and mantle structure beneath regional arrays (Unpublished doctoral dissertation). Columbia University.

Jin, G., & Gaherty, J. B. (2015). Surface wave phase-velocity tomography based on multichannel cross-correlation. *Geophysical Journal International*, *201*(3), 1383–1398. https://doi.org/10.1093/gji/ggv079

Kustowski, B., Ekström, G., & Dziewoński, A. (2008). Anisotropic shear-wave velocity structure of the earth's mantle: A global model. *Journal of Geophysical Research*, *113*, B06306. https://doi.org/10.1029/2007JB005169

Lebedev, S., & Nolet, G. (2003). Upper mantle beneath southeast Asia from s velocity tomography. *Journal of Geophysical Research*, *108*(B1), 2048. https://doi.org/10.1029/2000JB000073

Levshin, A. L., Barmin, M. P., Ritzwoller, M. H., & Trampert, J. (2005). Minor-arc and major-arc global surface wave diffraction tomography. *Physics of the Earth and Planetary Interiors*, *149*(3-4), 205–223.

Li, A., Forsyth, D. W., & Fischer, K. M. (2003). Shear velocity structure and azimuthal anisotropy beneath eastern north America from Rayleigh wave inversion. *Journal of Geophysical Research*, *108*(B8), 2362. https://doi.org/10.1029/2002JB002259

Li, X., & Romanowicz, B. (1996). Global mantle shear velocity model developed using nonlinear asymptotic coupling theory. *Journal of Geophysical Research*, *101*(B10), 22,245–22,272.

Lin, F.-C., & Ritzwoller, M. H. (2011). Helmholtz surface wave tomography for isotropic and azimuthally anisotropic structure. *Geophysical Journal International*, *186*(3), 1104–1120.

Lin, F.-C., Ritzwoller, M. H., & Snieder, R. (2009). Eikonal tomography: Surface wave tomography by phase front tracking across a regional broad-band seismic array. *Geophysical Journal International*, *177*(3), 1091–1110.

Luo, Y., Yang, Y., Zhao, K., Xu, Y., & Xia, J. (2015). Unraveling overtone interferences in love-wave phase velocity measurements by radon transform. *Geophysical Journal International*, *203*(1), 327–333.

Ma, Z., Masters, G., Laske, G., & Pasyanos, M. (2014). A comprehensive dispersion model of surface wave phase and group velocity for the globe. *Geophysical Journal International*, *199*(1), 113–135.

Masters, G., Woodhouse, J. H., & Freeman, G. (2011). Mineos v1.0.2 Retrieved from https://geodynamics.org/cig/software/mineos/

Matsuzawa, H., & Yoshizawa, K. (2019). Array-based analysis of multimode surface waves: Application to phase speed measurements and modal waveform decomposition. *Geophysical Journal International*, *218*(1), 295–312.

Moulik, P., & Ekström, G. (2014). An anisotropic shear velocity model of the earth's mantle using normal modes, body waves, surface waves and long-period waveforms. *Geophysical Journal International*, *199*(3), 1713–1738.

Nettles, M., & Dziewoński, A. M. (2011). Effect of higher-mode interference on measurements and models of fundamental-mode surface-wave dispersion. *Bulletin of the Seismological Society of America*, *101*(5), 2270–2280.

Nolet, G. (1975). Higher Rayleigh modes in western Europe. *Geophysical Research Letters*, *2*(2), 60–62.

Ritsema, J., Deuss, a. A., Van Heijst, H., & Woodhouse, J. (2011). S40rts: A degree-40 shear-velocity model for the mantle from new Rayleigh wave dispersion, teleseismic traveltime and normal-mode splitting function measurements. *Geophysical Journal International*, *184*(3), 1223–1236.

Selby, N. D., & Woodhouse, J. H. (2002). The q structure of the upper mantle: Constraints from Rayleigh wave amplitudes. *Journal of Geophysical Research*, *107*(B5), 2097. https://doi.org/10.1029/2001JB000257

Shapiro, N., & Ritzwoller, M. (2002). Monte-Carlo inversion for a global shear-velocity model of the crust and upper mantle. *Geophysical Journal International*, *151*(1), 88–105.

Shen, W., & Ritzwoller, M. H. (2016). Crustal and uppermost mantle structure beneath the United States. *Journal of Geophysical Research: Solid Earth*, *121*, 4306–4342. https://doi.org/10.1002/2016JB012887

Thatcher, W., & Brune, J. N. (1969). Higher mode interference and observed anomalous apparent love wave phase velocities. *Journal of Geophysical Research*, *74*(27), 6603–6611.

Tromp, J., Komatitsch, D., Hjörleifsdóttir, V., Liu, Q., Zhu, H., Péter, D., et al. (2010). Near real-time simulations of global CMT earthquakes. *Geophysical Journal International*, *183*(1), 381–389.

Visser, K., Lebedev, S., Trampert, J., & Kennett, B. (2007). Global Love wave over-tone measurements. *Geophysical Research Letters*, *34*, L03302. https://doi.org/10.1029/2006GL028671

Wagner, L., Forsyth, D. W., Fouch, M. J., & James, D. E. (2010). Detailed three-dimensional shear wave velocity structure of the northwestern United States from Rayleigh wave tomography. *Earth and Planetary Science Letters*, *299*(3-4), 273–284.

Weeraratne, D. S., Forsyth, D. W., Fischer, K. M., & Nyblade, A. A. (2003). Evidence for an upper mantle plume beneath the Tanzanian craton from Rayleigh wave tomography. *Journal of Geophysical Research*, *108*(B9), 2427. https://doi.org/10.1029/2002JB002273

Wessel, P., & Smith, W. H. (1998). New, improved version of generic mapping tools released. *Eos, Transactions American Geophysical Union*, *79*(47), 579–579.

Woodhouse, J. H., & Dziewonski, A. M. (1984). Mapping the upper mantle: Three-dimensional modeling of earth structure by inversion of seismic waveforms. *Journal of Geophysical Research*, *89*(B7), 5953–5986.

Xu, H., & Beghein, C. (2019). Measuring higher-mode surface wave dispersion using a transdimensional Bayesian approach. *Geophysical Journal International*, *218*(1), 333–353.

Yoshizawa, K., & Ekström, G. (2010). Automated multimode phase speed measurements for high-resolution regional-scale tomography: Application to North America. *Geophysical Journal International*, *183*(3), 1538–1558.

Zhou, Y., Nolet, G., Dahlen, F., & Laske, G. (2006). Global upper-mantle structure from finite-frequency surface-wave tomography. *Journal of Geophysical Research*, *111*, B04304. https://doi.org/10.1029/2005JB003677